Supplementary materials

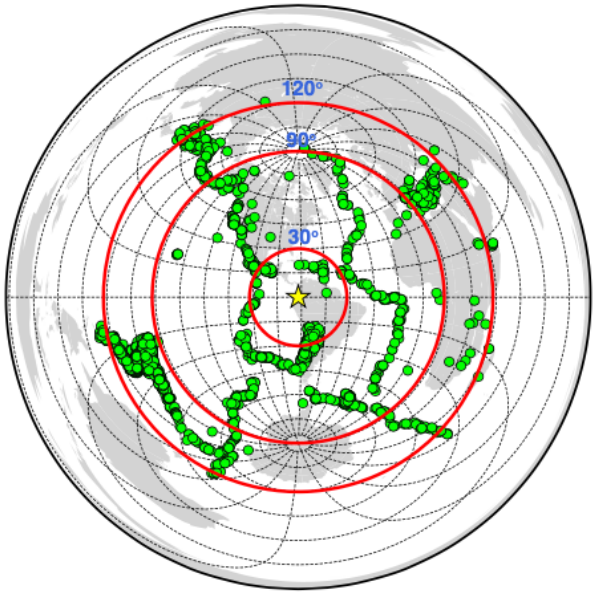

Figure S1. Distribution of teleseismic earthquakes used for Rayleigh-wave extraction. Earthquakes were selected with epicentral distances of 20°–120° and moment magnitudes $\geqslant$ 5.5. Red circles indicate epicentral distances of 30°, 90° and 120°. The yellow star denotes the center of the study region.

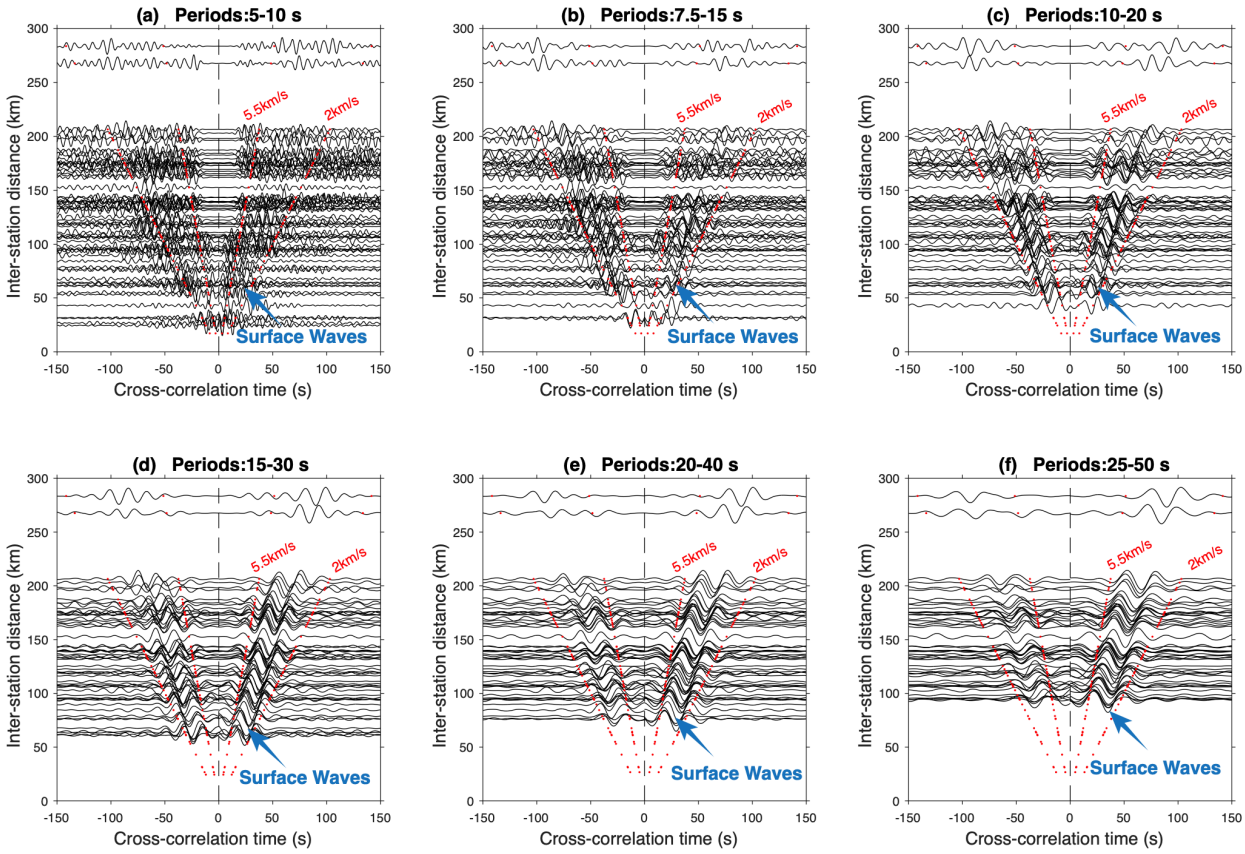

Figure S2. Ambient-noise cross-correlations for different period ranges from station XF. HB02 to all receivers. Symmetric Rayleigh-wave signals are indicated by blue arrows and annotated labels. Red dashed lines mark the estimated Rayleigh-wave arrival time range assuming shear velocities of 5.5 km/s and 2 km/s, respectively.

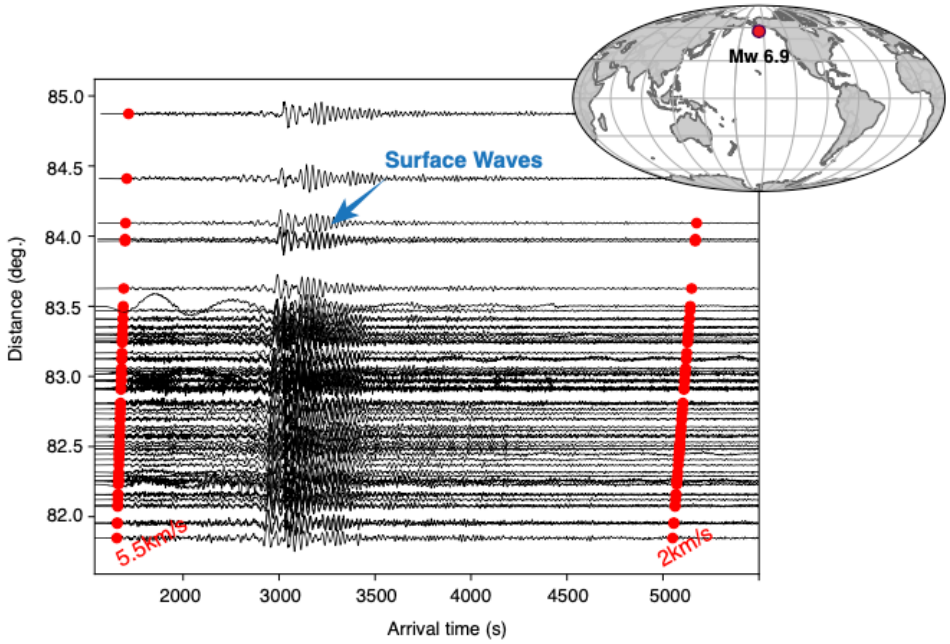

Figure S3. Teleseismic surface-wave recordings across the study region for an Mw 6.9 earthquake on October 11th, 2010. The event location is shown in the inset map (upper right). Surface-wave signals are indicated by blue arrows and annotated labels. Red dots mark the expected Rayleigh-wave arrival time range, estimated assuming shear velocities of 5.5 and 2.0 km/s, respectively. Waveforms are bandpass filtered over periods of 5-300 s.

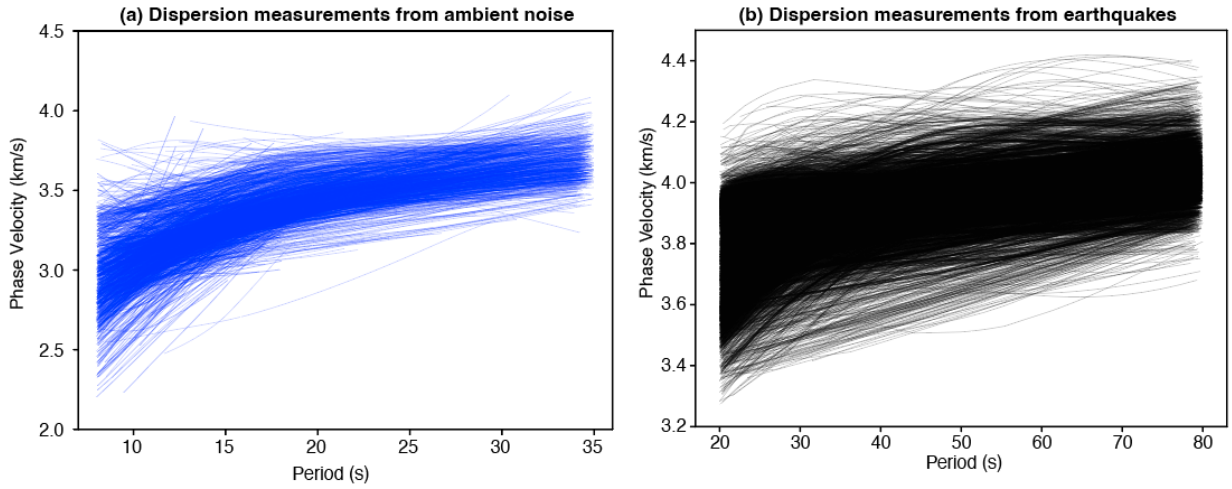

Figure S4. Phase-velocity dispersion measurements after quality control. (a) Phase-velocity dispersion curves measured from ambient-noise cross-correlations. (b) Phase-velocity dispersion curves measured from teleseismic surface waves. Only measurements with signal-to-noise ratios (SNR) > 5 for ambient noise and > 10 for teleseismic data were retained. SNR is defined as the ratio of peak signal amplitude to root-mean-square noise, following Bensen et al. (2007). The Rayleigh-wave signal window is defined using shear velocities of 5.5 km/s and 2 km/s. The noise window is defined as the 100 s after the main signals.

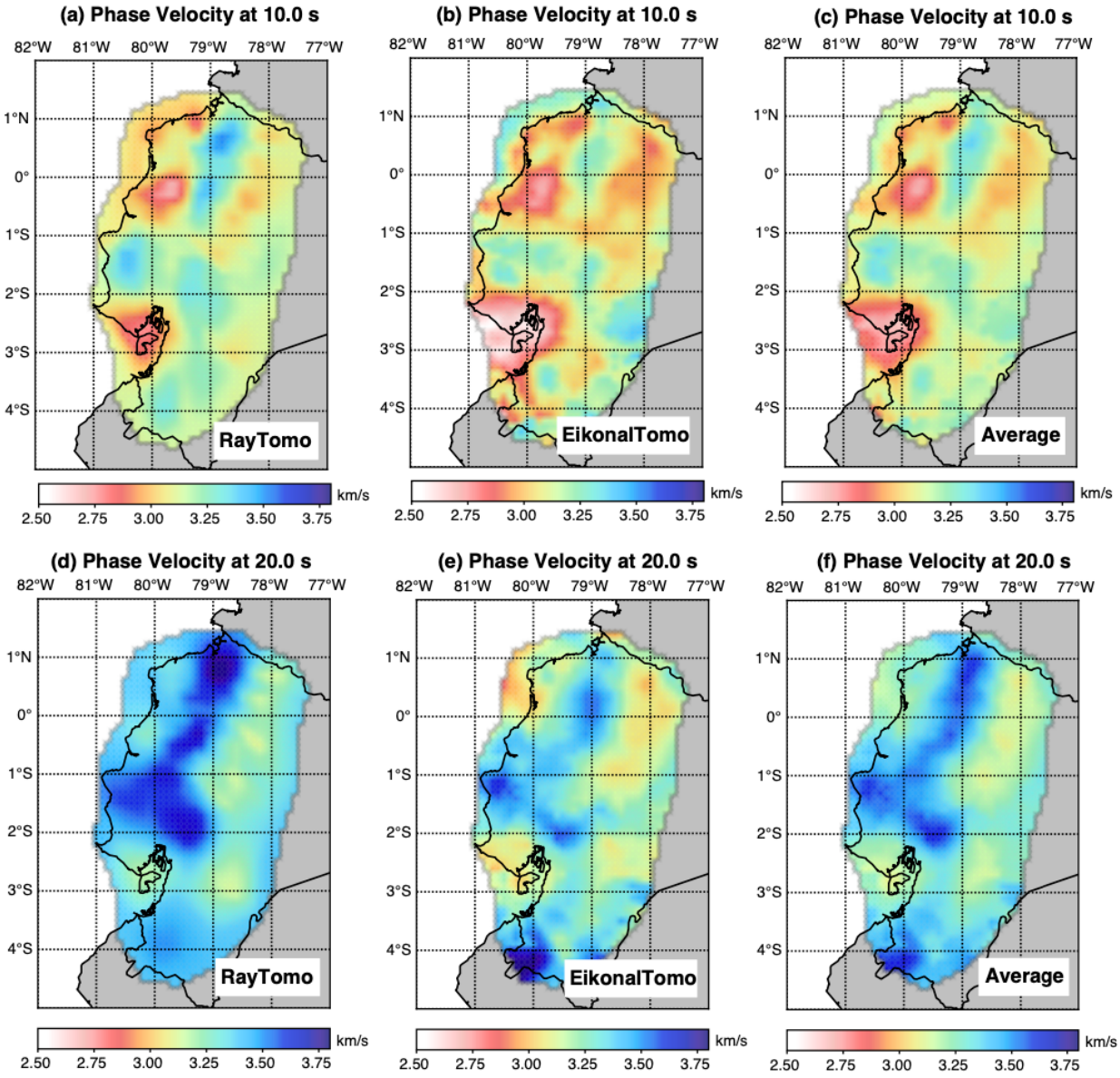

Figure S5. Comparison of phase-velocity maps derived using different inversion methods. (a–c) Phase-velocity maps at a period of 10 s obtained from ray-based tomography (RayTomo; Barmin et al., 2001), Eikonal tomography (EikonalTomo; Lin et al., 2009), and their average. (d–f) As in (a–c), but for a period of 20 s.

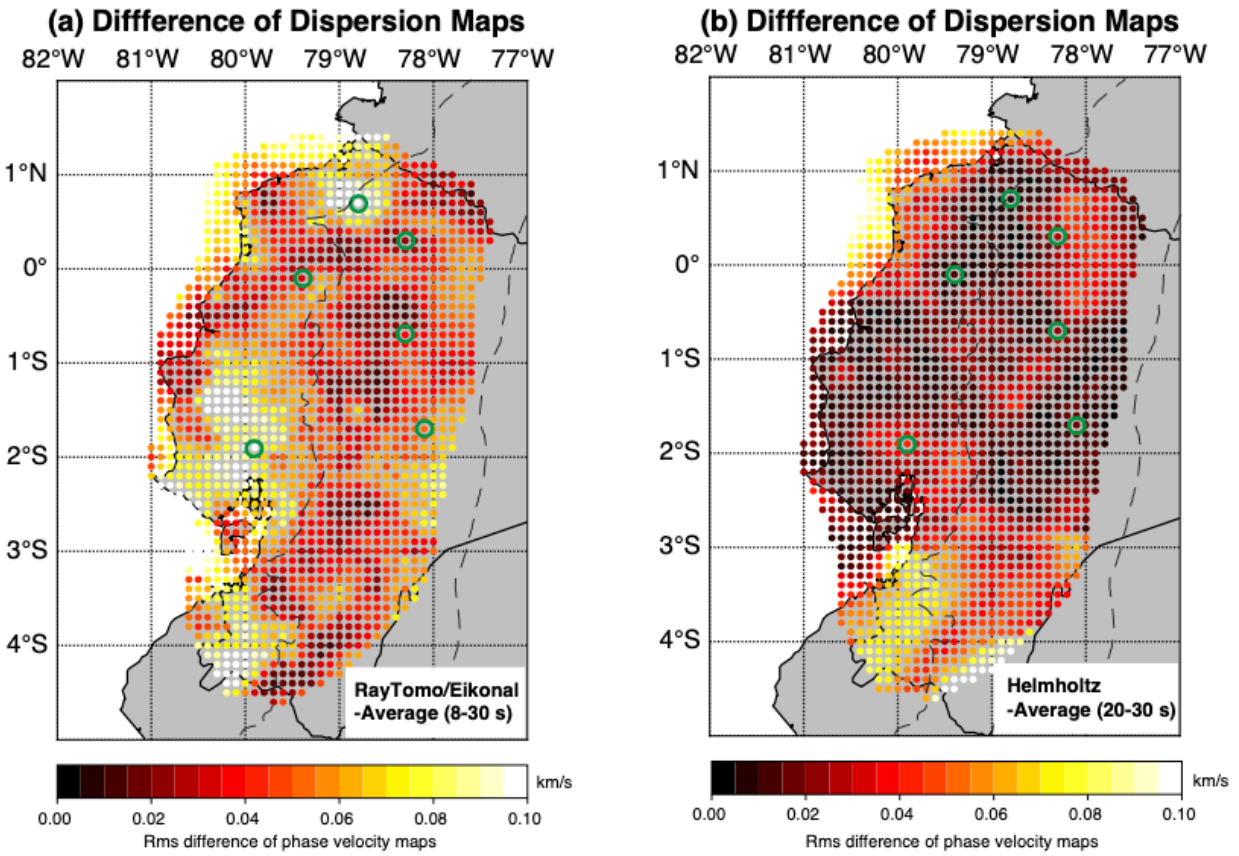

Figure S6. Comparison of phase-velocity models derived using different datasets and methods. (a) Root-mean-square (RMS) differences between phase-velocity maps at periods of 8-30 s obtained using ray-based tomography (RayTomo; Barmin et al., 2001) or Eikonal tomography (EikonalTomo; Lin et al., 2009) and the average of the two models. (b) RMS differences between phase-velocity maps at periods of 20-30 s derived from ambient-noise and teleseismic surface-wave data. Phase-velocity maps from ambient noise represent the average of results from ray-based tomography and Eikonal tomography. Phase-velocity maps from teleseismic surface waves are inverted by Helmholtz tomography (Lin et al., 2011). The Green circles mark the locations of phase velocity dispersion curves shown in Figure S7.

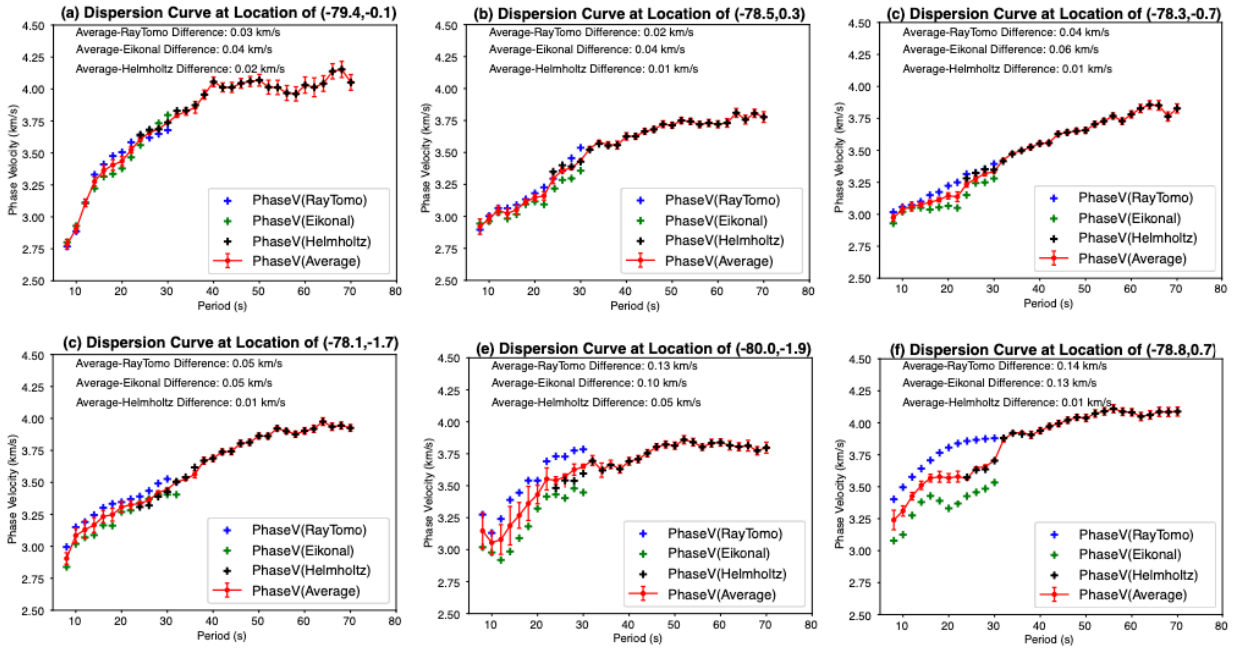

Figure S7. Examples of Rayleigh-wave phase velocity dispersion curves in different locations. The locations are marked in Figure S6. Green and blue crosses represent phase velocities inverted by ray-based tomography (RayTomo; Barmin et al. 2001) and Eikonal tomography (EikonalTomo; Lin et al., 2009) based on ambient noise data, and black crosses represent phase velocities inverted by Helmholtz tomography (HelmholtzTomo; Lin et al., 2011) based on teleseismic surface wave data.

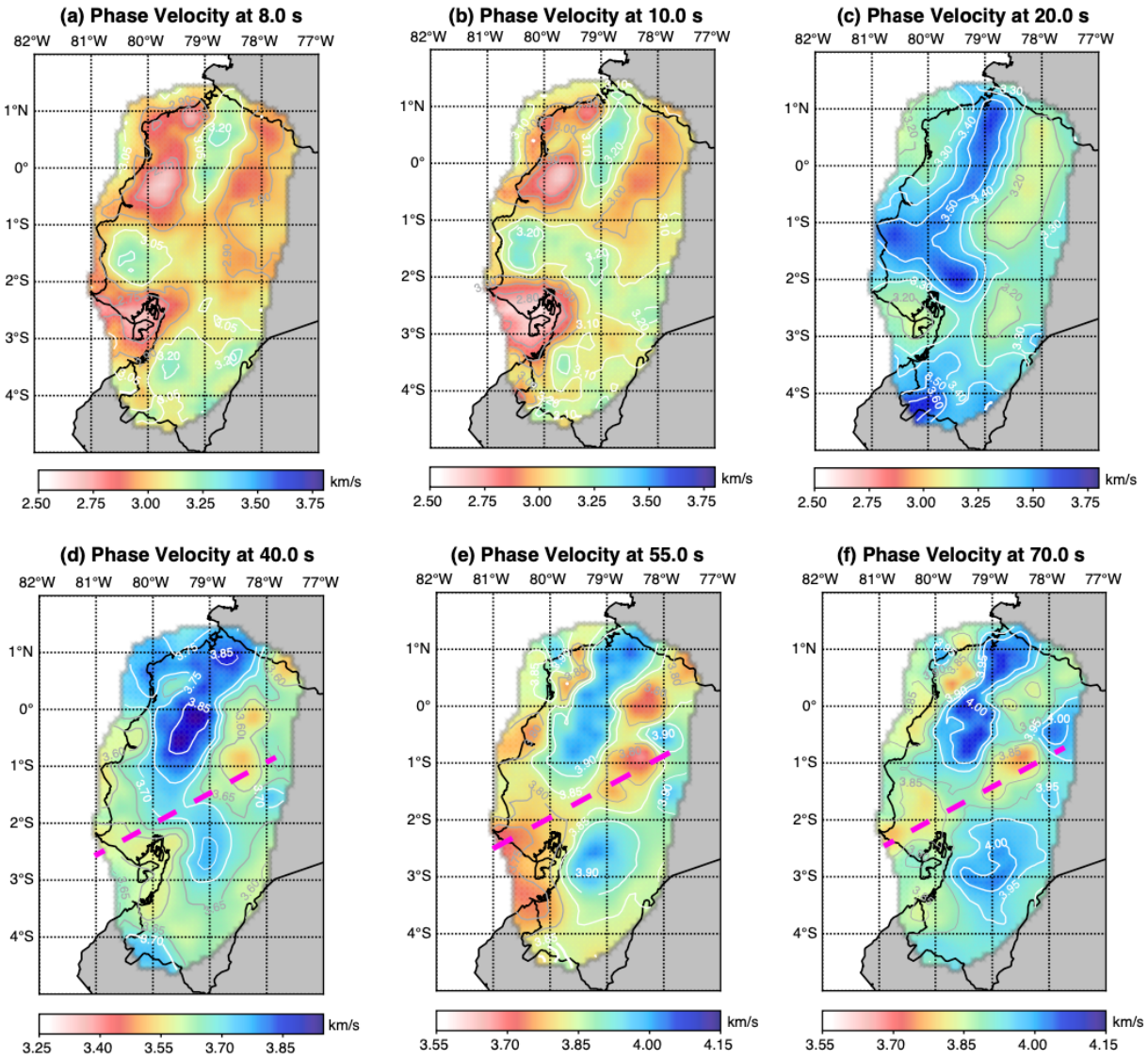

Figure S8. Phase-velocity maps at multiple periods. Gray and white contours delineate relatively low- and high-velocity anomalies, respectively. The red dashed line marks the inferred surface projection of the subducting Grijalva Fracture Zone, modified from Yepes et al. (2016).

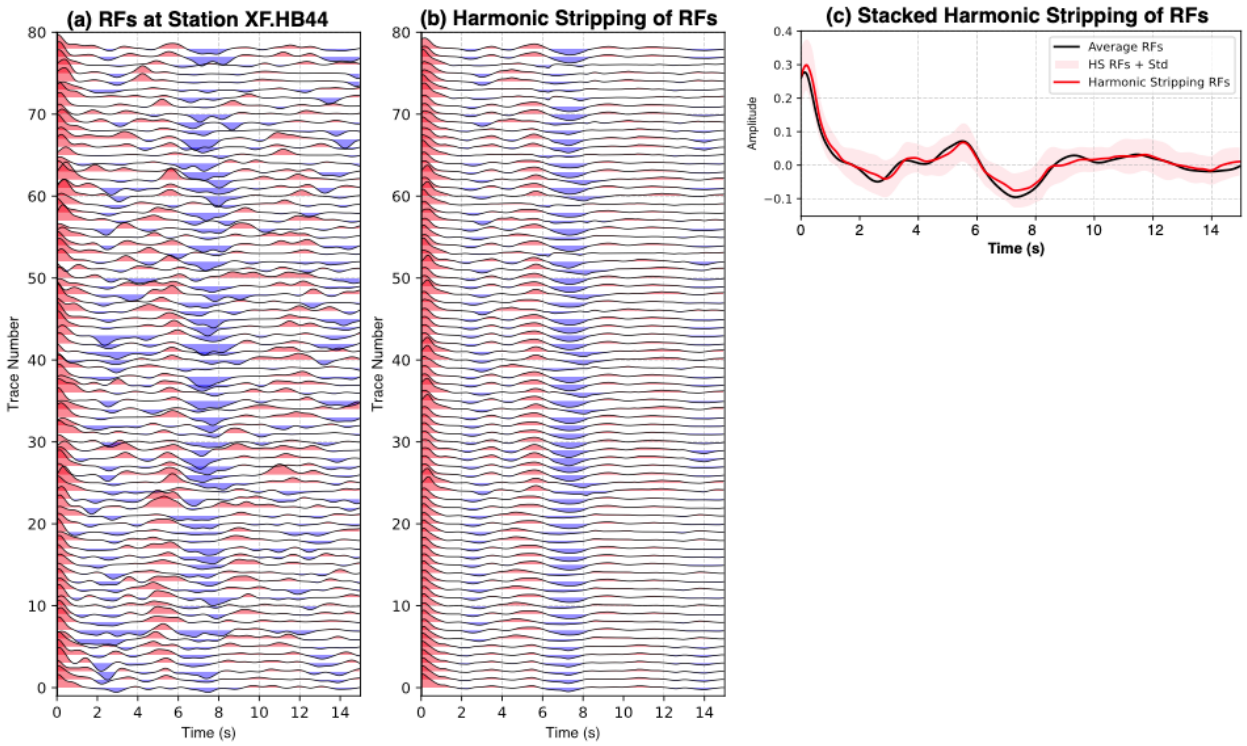

Figure S9. Example of the azimuthally independent component of receiver functions (RFs) extracted using the harmonic stripping method. (a) Selected RFs recorded at station XF.HB44. The RFs are normalized by the maximum amplitude of the P arrival at 0 s. Positive amplitudes are filled in red, and negative amplitudes are filled in blue. (b) Azimuthally independent component of the RFs extracted using the harmonic stripping method. (c) Stacked azimuthally independent component (red) and its uncertainty (red shading). The black curve shows the stacked RF obtained directly from the RFs in panel (a).

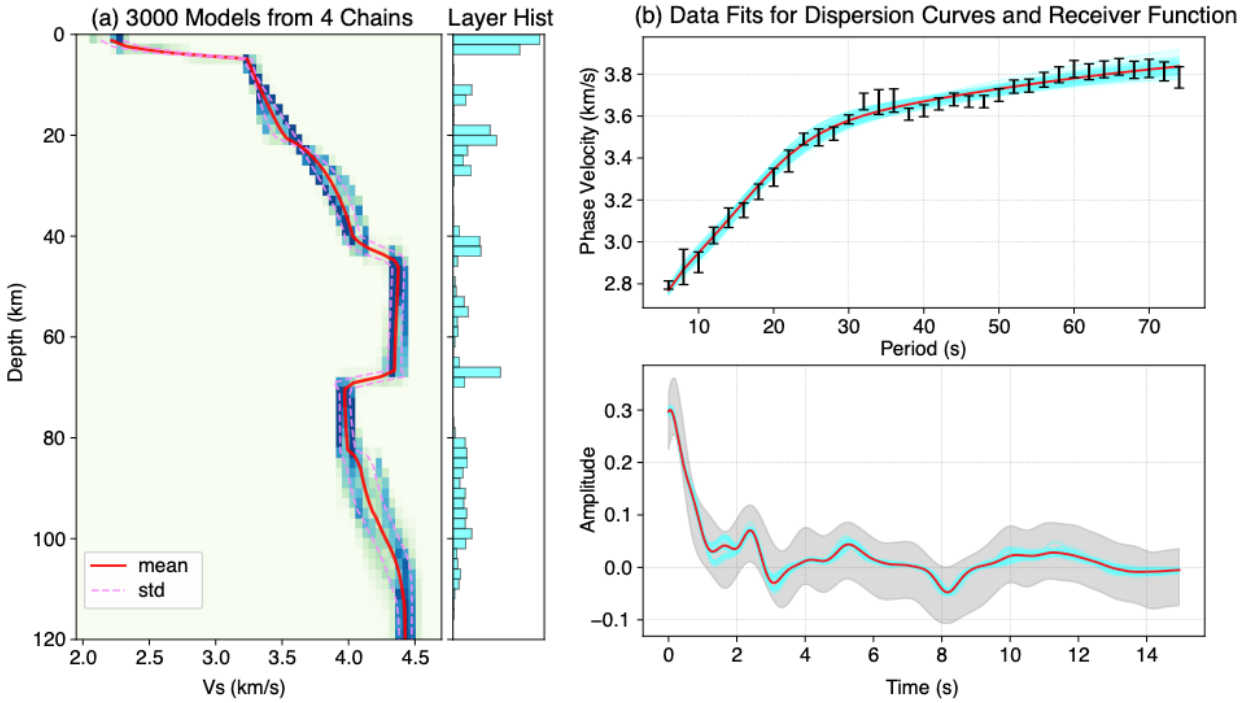

Figure S10. Example of the joint inversion of a Rayleigh-wave dispersion curve and a receiver function (RF) using a trans-dimensional Bayesian Markov chain Monte Carlo (McMC) framework. (a) Inverted 1-D shear-wave velocity profile (left) and histogram of the inferred number of layers (right) at 80.2°W, 0.2°S. The background color in the left panel indicates the posterior probability density of shear-wave velocity as a function of depth based on the final 3000 randomly sampled models. The red solid line shows the posterior mean model, and the pink dashed lines indicate one standard deviation. (b) Comparison between the observed and synthetic Rayleigh-wave dispersion curves. Black error bars denote the observed dispersion curve and its uncertainty. Thin cyan lines represent synthetic dispersion curves predicted from the final 3000 sampled models, and the red line represents the prediction from the posterior mean model. (c) Comparison between the observed and synthetic RFs. The black line shows the stacked RF at station XF.HB44, and the gray shading indicates its uncertainty. Thin cyan lines represent synthetic RFs predicted from the final 3000 sampled models, and the red line represents the synthetic RF predicted from the posterior mean model.

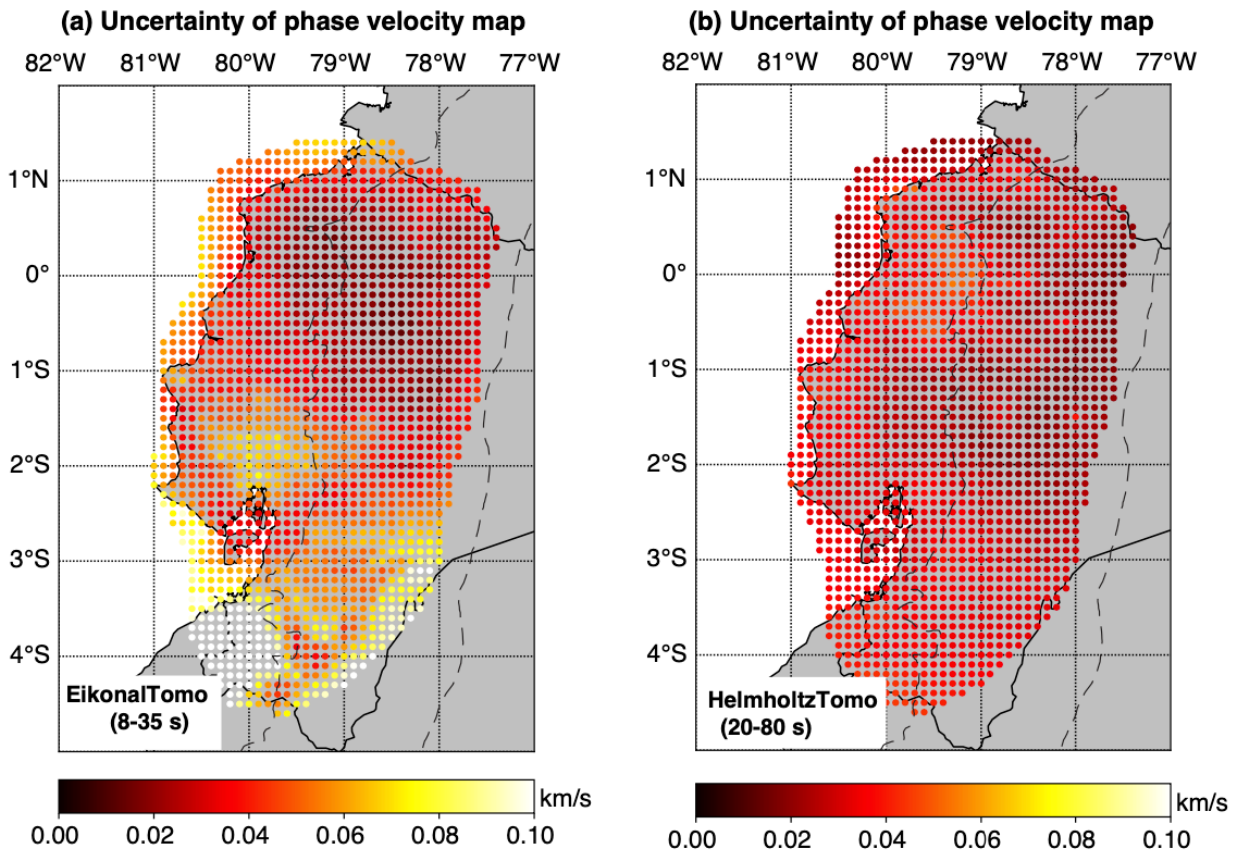

Figure S11. Inversion uncertainty of phase-velocity map from Eikonal and Helmholtz tomography. (a) Inversion uncertainty of Eikonal tomography for ambient noise data at short periods of 8-30 s. (b) Inversion uncertainty of Helmholtz tomography for teleseismic surface waves at long periods of 20-80 s. The uncertainty is calculated by the standard deviation of the mean slowness measurements obtained from Eikonal and Helmholtz tomography.

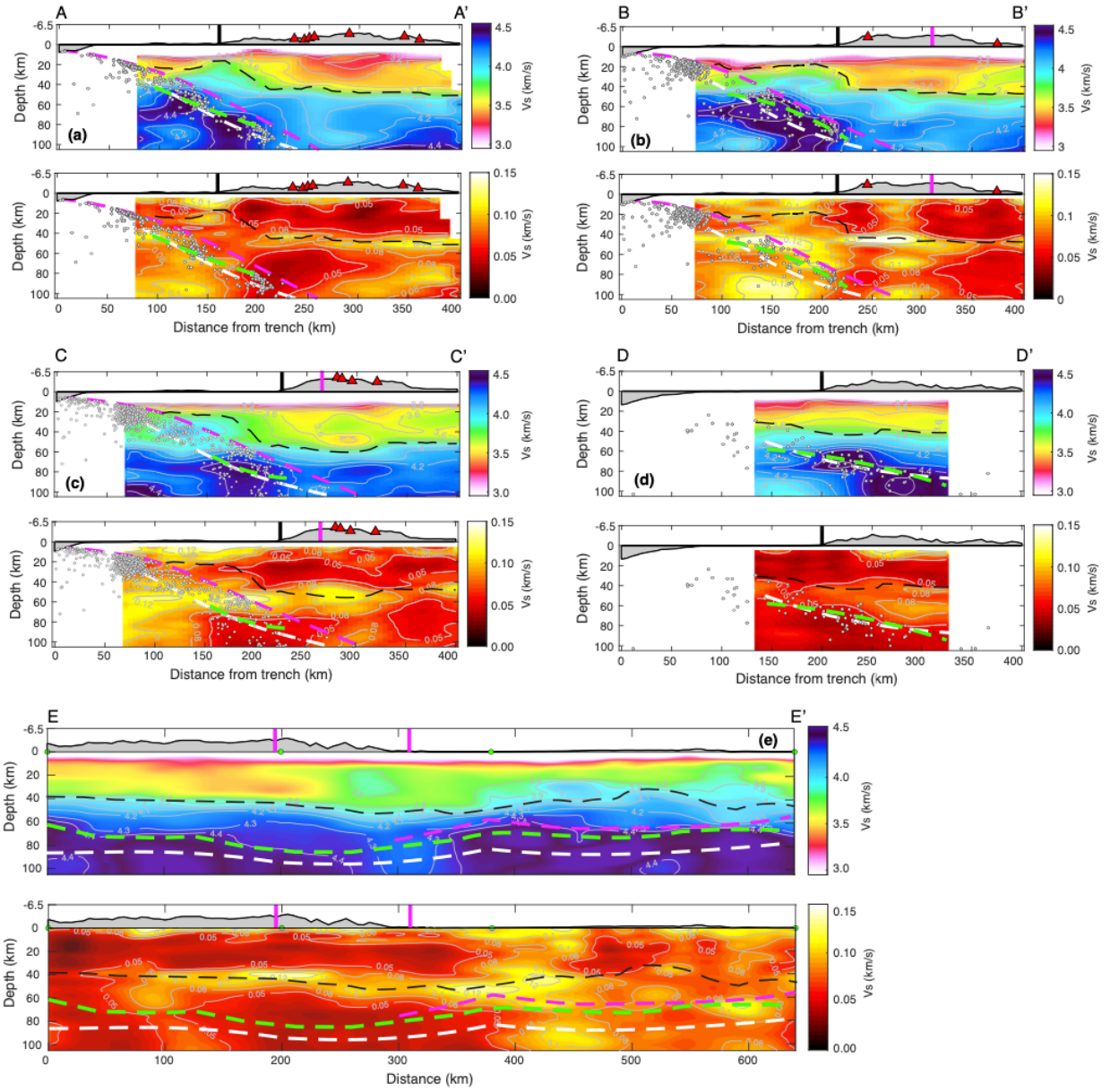

Figure S12. Cross-sections of the shear-wave velocity model and associated inversion uncertainties. (a-d) Shear-wave velocity models (top) and their corresponding inversion uncertainties (bottom) along trench-normal profiles. Profile locations are shown in Fig. 2a. Black dashed lines indicate the base of the accreted oceanic terrane crust beneath the forearc and the Moho of the South American continental crust beneath the Cordillera. Green dashed lines indicate the slab interface inferred from our tomographic model, while pink and white dashed lines represent the slab interfaces from Font et al. (2013) and Hayes et al. (2018), respectively. Triangles denote Holocene volcanoes in the northern Andes. (e) Same as (a-d), but for a profile oriented along the slab. The profile location is shown in Fig. 4a.

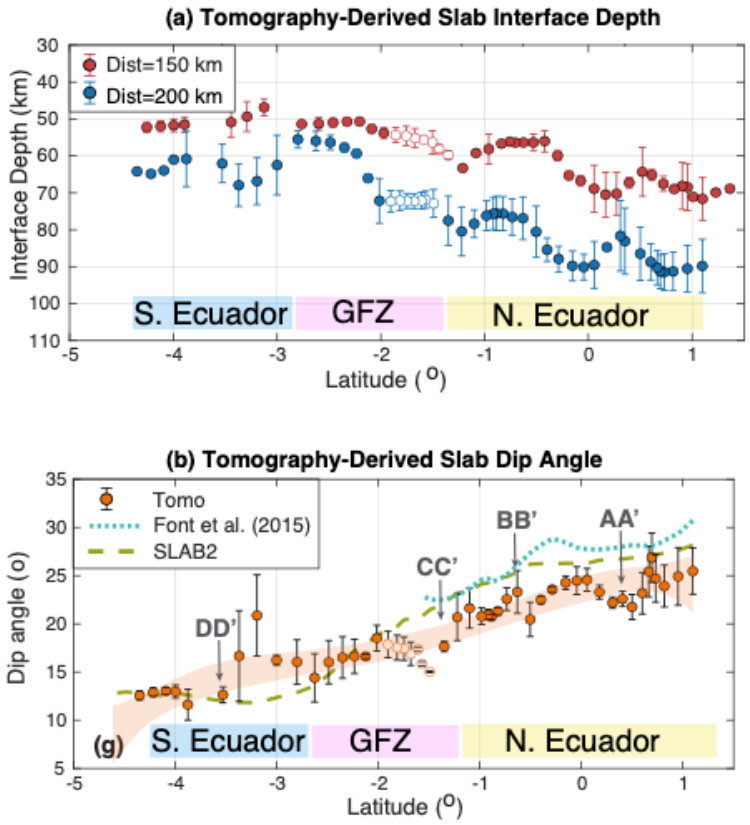

Figure S13.Along-strike variations in tomography-derived slab interface depth and dip angle. (a) Slab interface depths at trench-normal distances of 150 km (red circles) and 200 km (blue circles), with error bars indicating uncertainties. Solid circles indicate interface picks from strong shear-wave velocity larger than 0.2 km/s, while open circles mark the interce picks with relatively weak gradients of 0.1-0.2 km/s. Colored shaded regions along the bottom indicate the southern Ecuador, Grijalva Fracture Zone (GFZ) continuation, and northern Ecuador domains. (b) Slab dip angles derived from the tomographic model (orange circles with error bars). Dip angles are calculated at 5-km intervals from the trench, with the mean and standard deviation representing the estimated dip angle and its uncertainty, respectively. Cyan dotted and olive dashed lines show slab dip angles derived from the models of Font et al. (2013) and Slab2 (Hayes et al., 2018), respectively.

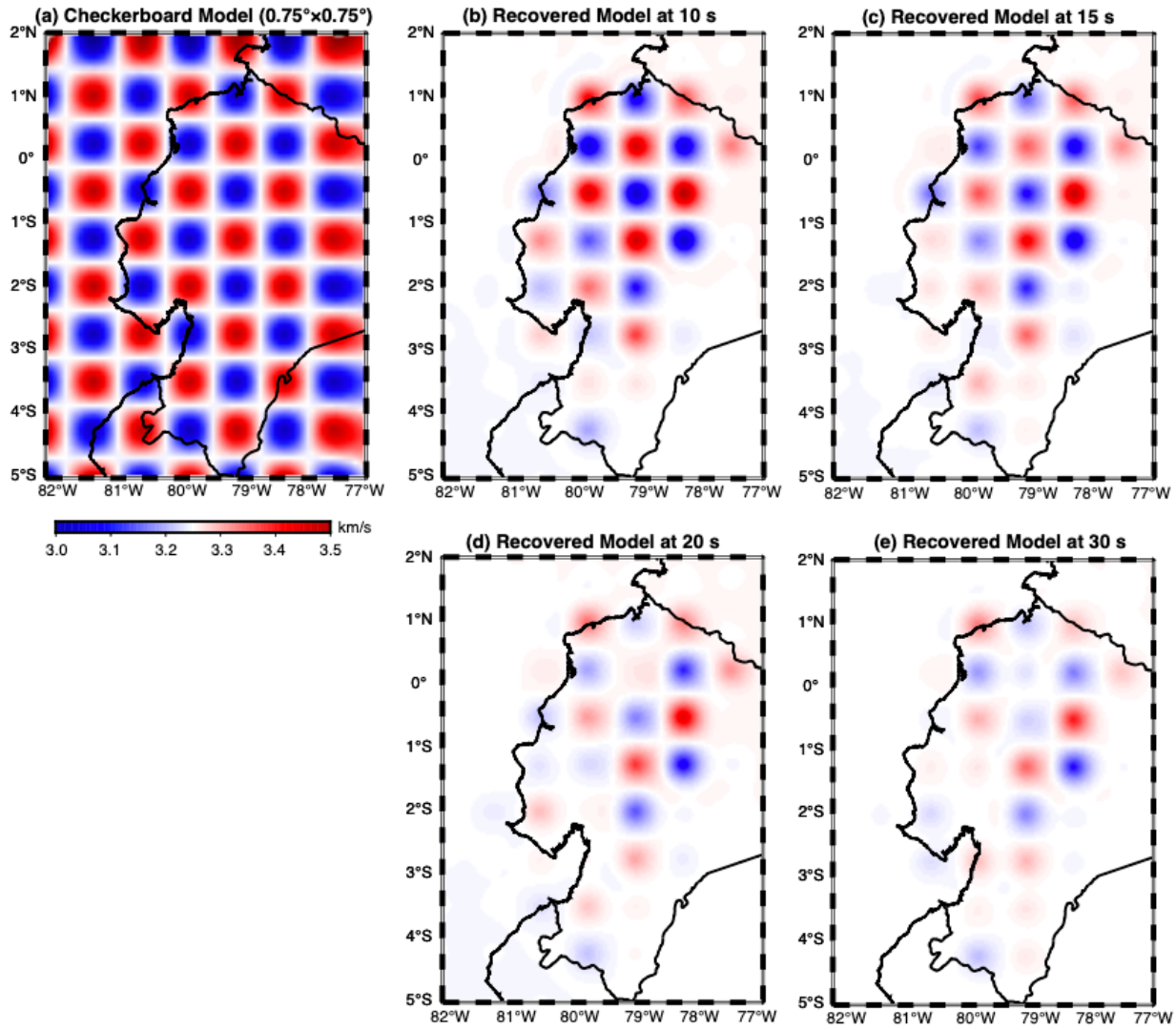

Figure S14. Checkerboard resolution tests for phase-velocity tomography based on ambient-noise Rayleigh-wave dispersion data at periods of 8-30 s. (a) Input checkerboard model. Velocity perturbations vary by ±8% relative to the reference velocity of 3.25 km/s. The horizontal cell size is 0.75° × 0.75°. (b–e) Recovered models using dispersion data at different periods. Longer periods primarily sample greater depths and therefore evaluate the resolution of deeper structures.

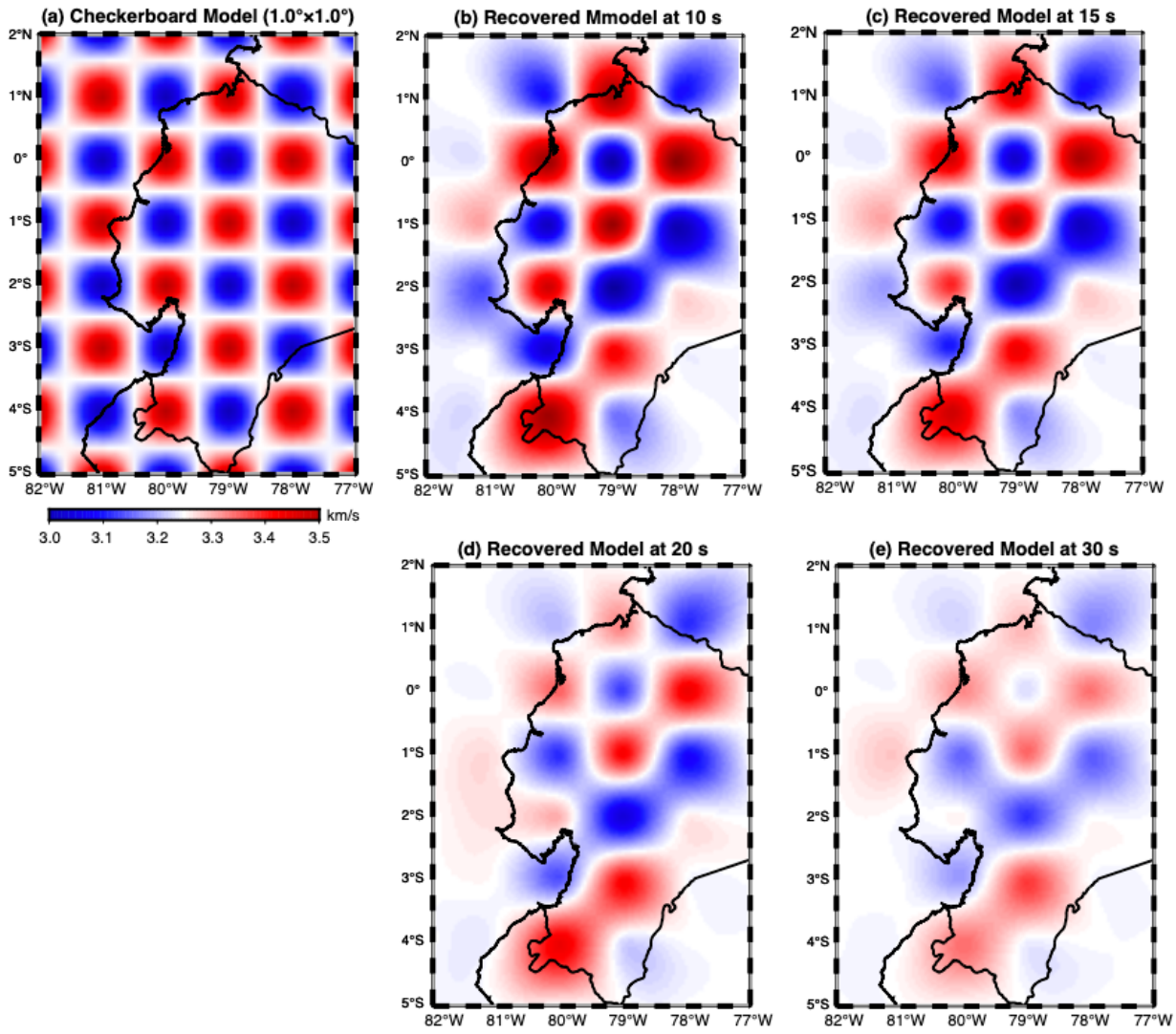

Figure S15.Same to Figure S14, except for the cell size in the input model is 1.0º ×1.0º.

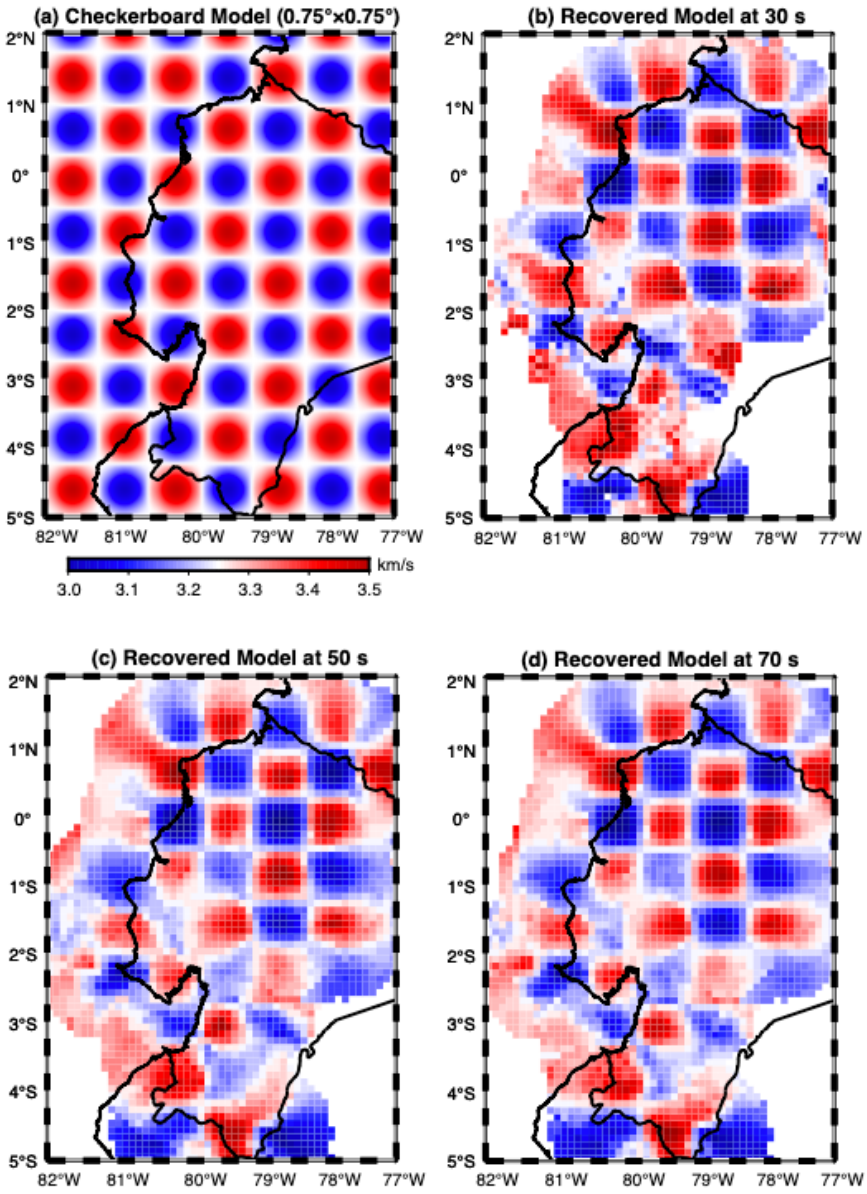

Figure S16. Checkerboard resolution tests for phase-velocity tomography based on teleseismic earthquake Rayleigh-wave dispersion data at periods of 20–80 s. (a) Input checkerboard model. Velocity perturbations vary by ±8% relative to the reference velocity of 3.25 km/s. The horizontal cell size is 0.75° × 0.75°. (b–e) Recovered models using dispersion data at different periods.

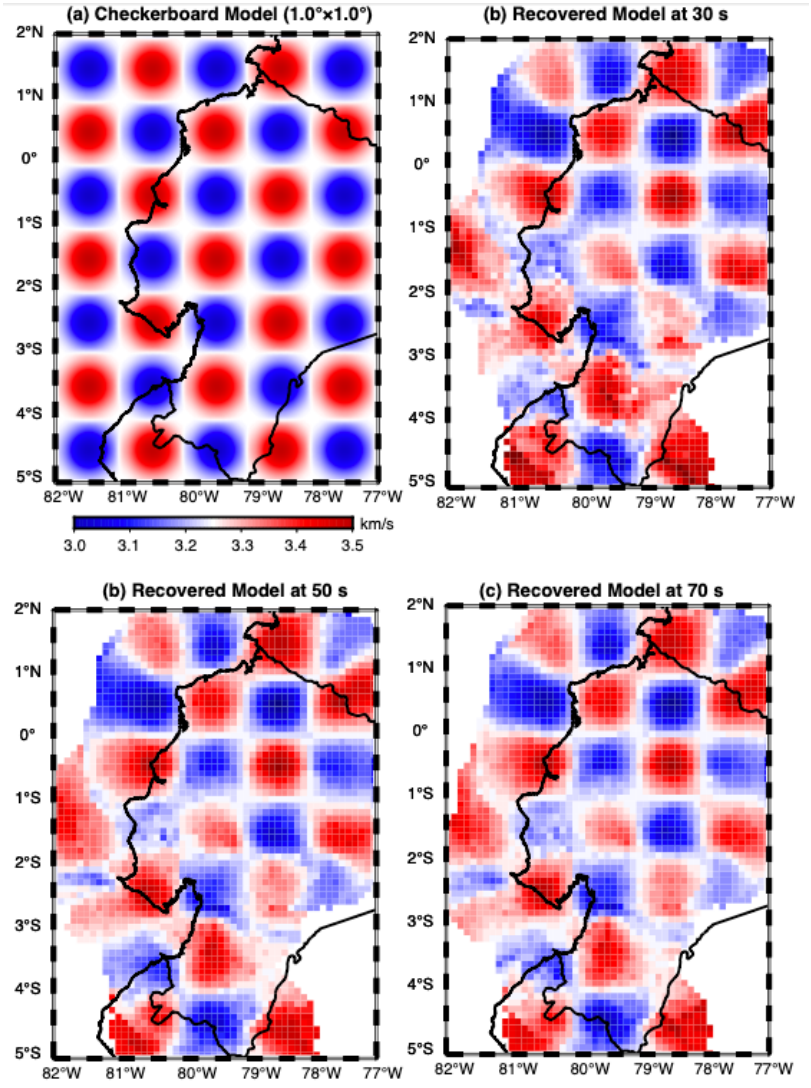

Figure S17. Same to Figure S16, except for the cell size in the input model is 1.0°×1.0°.

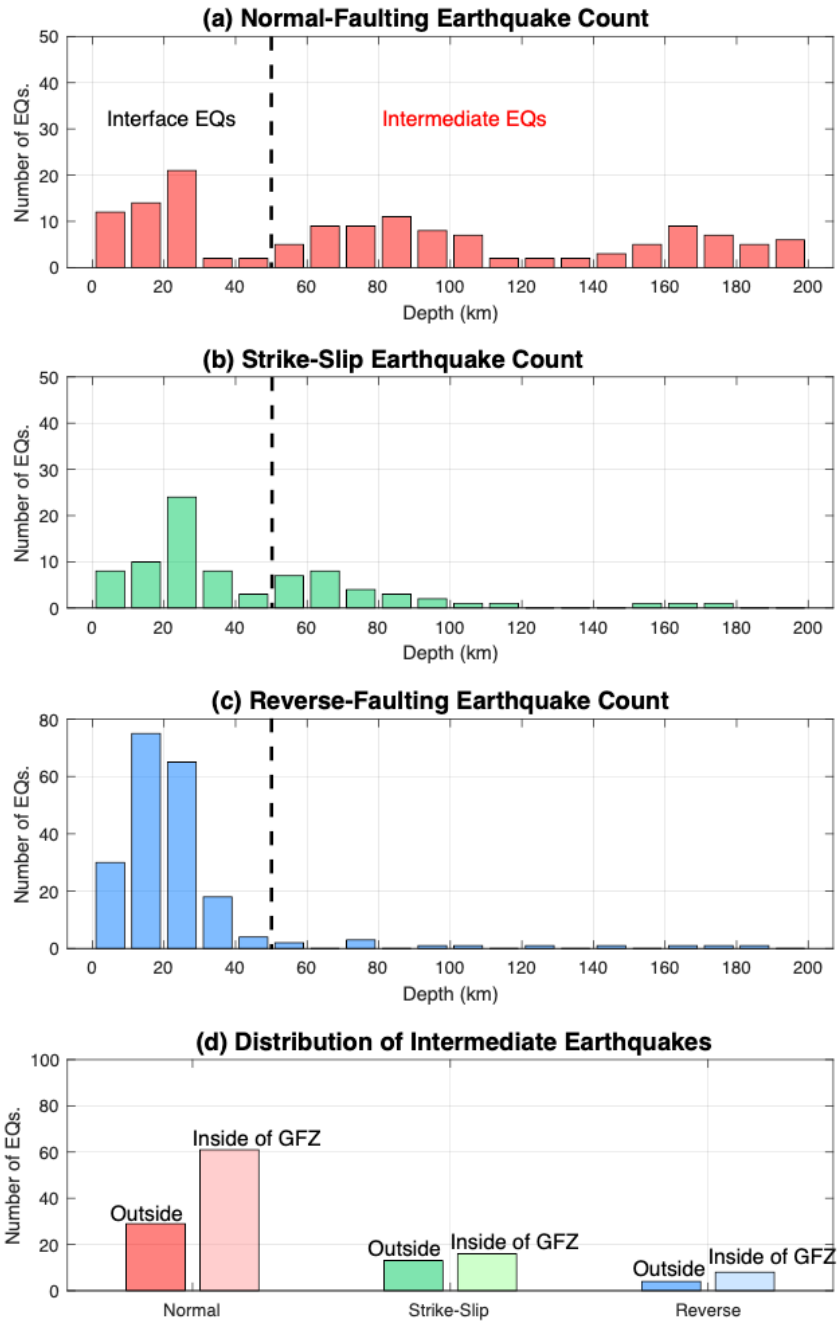

Figure S18.Depth distributions of intraslab earthquakes with different focal-mechanism types. The spatial distributions of earthquakes with different focal mechanisms are shown in Figure 4c. (a) Depth distribution of normal-faulting earthquakes. The black dashed line at 50 km depth marks the threshold used to distinguish shallow from intermediate-depth earthquakes in this study. (b–c) Same as (a), but for strike-slip and reverse-faulting earthquakes, respectively. (d) Comparison of the numbers of intermediate-depth earthquakes (>50 km) within and outside the inferred inland continuation zone of the Grijalva Fracture Zone (GFZ), grouped by focal-mechanism type: normal faulting (red), strike-slip (green), and reverse faulting (blue).

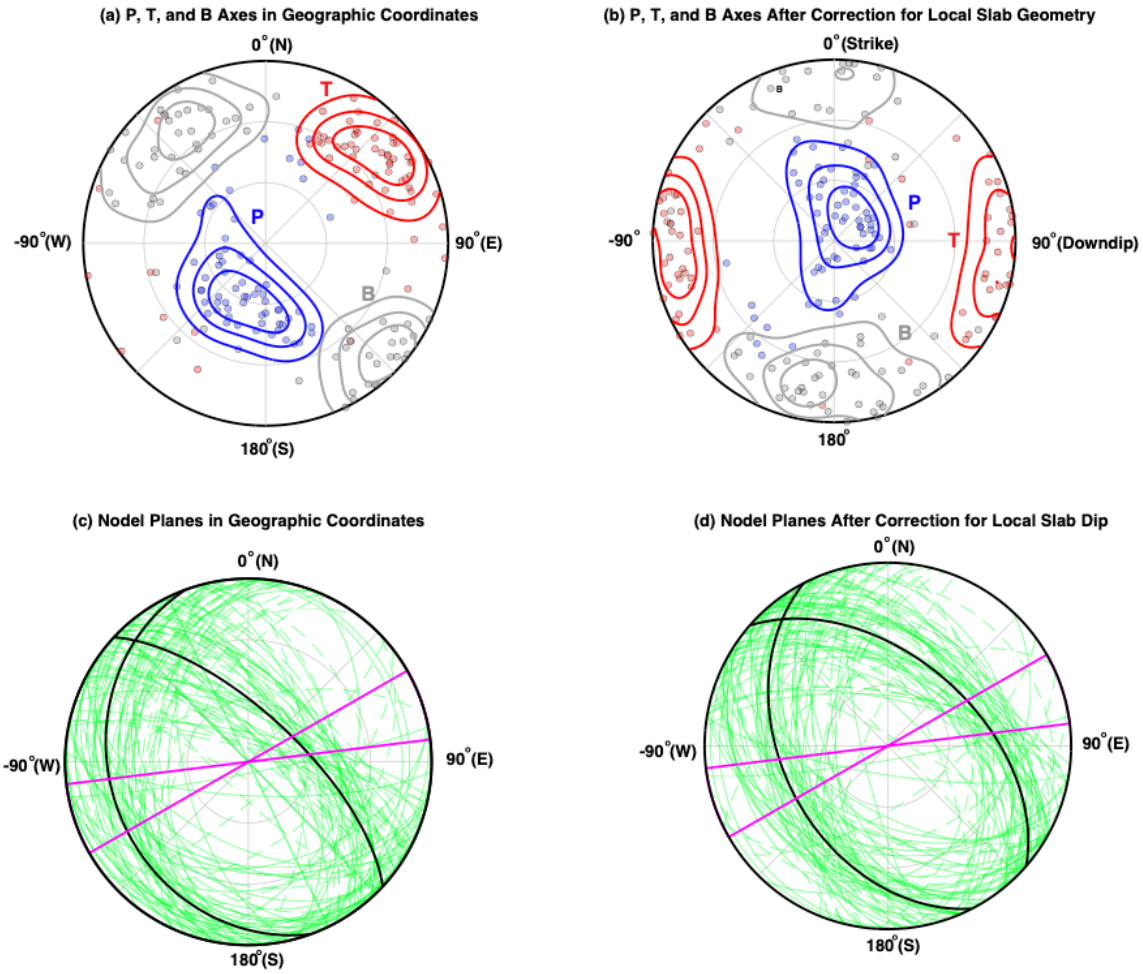

Figure S19. Stereonet distributions of P, T, and B axes and nodal planes for normal-faulting intraslab earthquakes. The spatial distribution of these earthquakes is shown in Figure 4c–e. (a) P, T, and B axes in geographic coordinates. (b) P, T, and B axes in slab-relative coordinates after correction for local slab geometry. In the slab-relative reference frame, ±90° represents the downdip/updip direction, 0° and 180° are parallel to the local slab strike, and the center of the stereonet represents the slab-normal direction. Blue, red, and gray dots and corresponding density contours represent the P, T, and B axes, respectively. (c) Nodal planes in geographic coordinates. Green great circles represent individual nodal planes, and the black great circle indicates their mean orientation. Pink lines indicate the strike directions of the northern and southern boundaries of the inferred inland continuation of the Grijalva Fracture Zone (GFZ). (d) Same as (c), but with the nodal planes corrected for local slab dip.

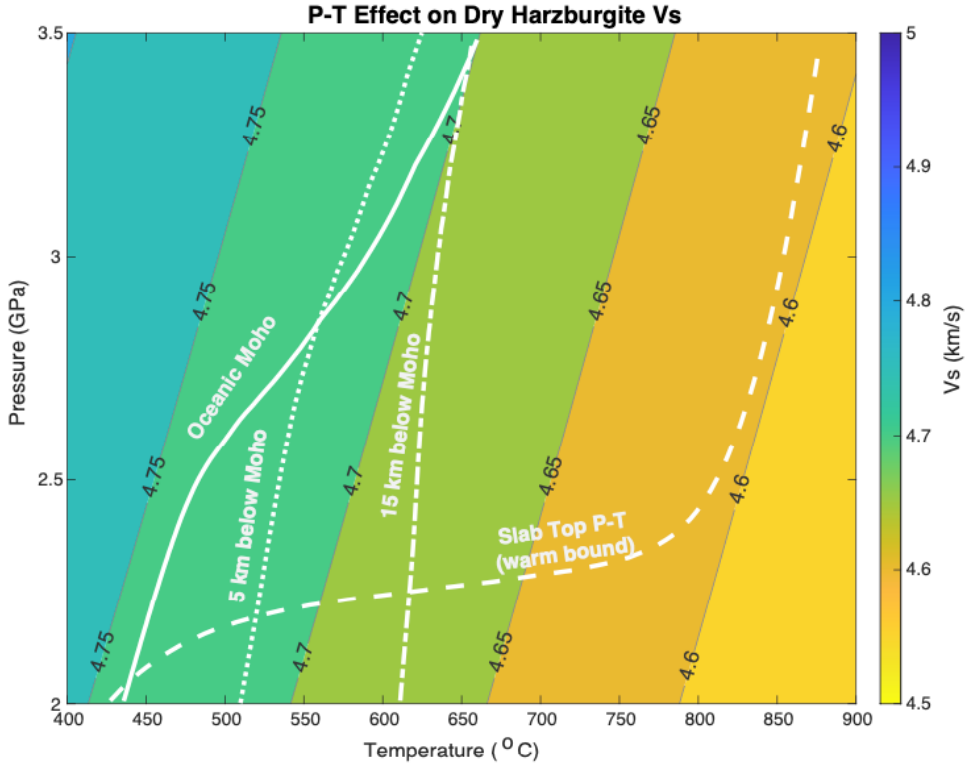

Figure S20. P–T effect on the shear-wave velocity of dry harzburgite in subducting slab mantle. Shear-wave velocity (Vs) is calculated over pressures of 2.0–3.5 GPa and temperatures of 400–900 °C using the dry harzburgite reference assemblage of Hacker et al. (2003) and the mineral-physics formulation of Abers and Hacker (2016). White solid, dashed, and dash-dotted lines show P–T trajectories along the slab top, oceanic Moho, 5 km and 15 km below the oceanic Moho, respectively, from the thermal model for Ecuador. The slab-top trajectory is shown as a warm thermal bound. Dry harzburgite retains Vs >4.6 km/s across the modeled P–T range, substantially higher than the observed SLVZ velocities in Figures 4a and 5a, indicating that P–T effects on dry harzburgite alone cannot account for the SLVZ.

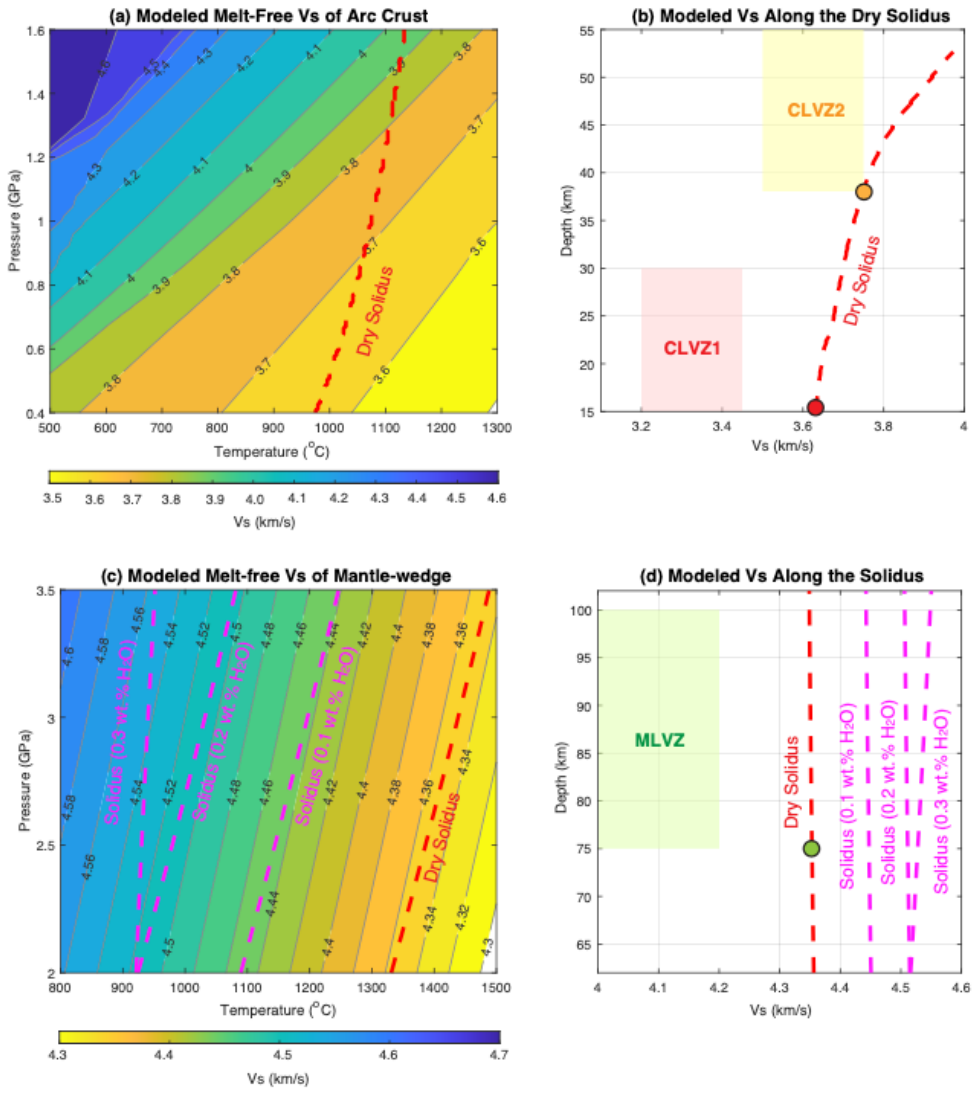

Figure S21. Comparison of observed crustal and upper-mantle low-velocity anomalies beneath the Ecuadorian volcanic arc with modeled melt-free shear-wave velocities (Vs). (a) Pressure–temperature–shear-wave velocity (P–T–Vs) diagram for melt-free crustal rocks at 0.4–1.6 GPa and 500–1300 °C. Vs is calculated based on bulk compositions of Ecuadorian Cordillera rocks from Hughes and Pilatasig (2002) using Perple_X software and the mineral-physics formulation of Abers and Hacker (2016). The red dashed curve indicates the predicted dry solidus. (b) Modeled melt-free Vs along the dry solidus compared with the observed Vs ranges of the upper–middle-crustal (CLVZ1; red shading) and lower-crustal (CLVZ2; yellow shading) low-velocity zones. (c) P–T–Vs diagram for melt-free upper-mantle rocks at 2–3.5 GPa (~62–105 km depth) and 800–1500 °C. Vs is calculated using representative lherzolite mineral assemblages for the mantle wedge from Hacker et al. (2003) and Bernardino et al. (2019). Red and magenta dashed curves indicate the dry solidus and hydrous solidi for different H_2O contents, respectively, following Katz et al. (2003). (d) Modeled melt-free Vs along the dry and hydrous solidi compared with the observed Vs range of the upper-mantle low-velocity zone (MLVZ; green shading) beneath the volcanic arc. Red

and orange dots mark the minimum melt-free Vs along the dry solidus at the corresponding depth ranges of CLVZ1, CLVZ2, and MLVZ.

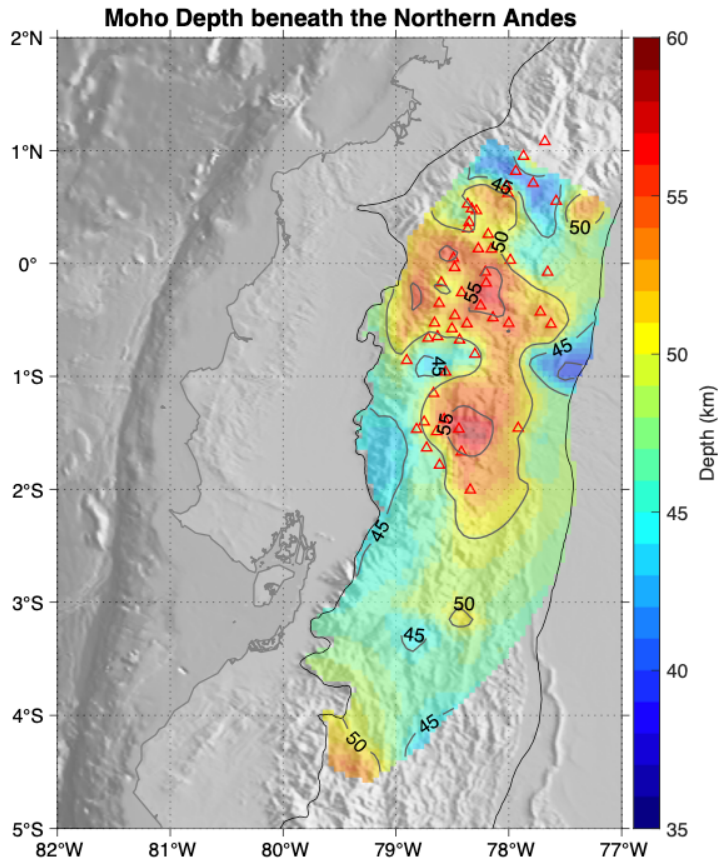

Figure S22. The Moho depth below sea level estimated from the maximum positive vertical Vs gradient. The black thin line marks the Cordillera region. The red triangles mark the location of Holocene volcanoes.

Table S1. Representative major-element compositions used for estimating melt fractions in the Ecuadorian crust and mantle wedge.

Bulk Composition (wt%)	Cordillera	Arc volcanic complexes	Primitive mantle-derived melts
---	Hughes & Pilatasig (2002)	Nauret et al. (2018) Samaniego et al. (2011) Samaniego et al. (2010)	Narvaez et al. (2018)
SiO2	54.3	59.1	48.0
TiO2	0.9	0.8	0.75
Al2O3	15.3	16.4	15.5
Fe2O3*	10.6	6.8	13.05
MnO	0.2	0.1	0.1
MgO	6.8	4.3	8.83
CaO	8.4	6.4	8.58
Na2O	3.0	4.0	3.40
K2O	0.4	1.9	1.46
P2O5	0.1	0.2	0.29
Total	100	100.0	100.0